Synthetic iron pyrite across length scales: Interfacial defects and macroscopic properties

Journal:	*CrystEngComm*
Manuscript ID	CE-ART-01-2019-000145.R1
Article Type:	Paper
Date Submitted by the Author:	22-Apr-2019
Complete List of Authors:	Roberts, Dennice; University of Colorado at Boulder, Mechanical Engineering Russek, Stephen; NIST Boulder Laboratories Stoldt, C. R. ; University of Colorado Boulder, Mechanical Engineering

SCHOLARONE™
Manuscripts

Journal Name

Synthetic iron pyrite across length scales: Interfacial defects and macroscopic properties[†]

Dennice M. Roberts,[a] Stephen E. Russek,[b] and Conrad R. Stoldt[*a]

Iron pyrite (FeS_2) has long represented a materials science challenge because of the immense sensitivity of its macroscopic behavior to defect structure. Research along this vein has primarily focused on the deleterious effects of sulfur vacancies on optical and electronic properties that prevent the material from being successfully integrated into photovoltaic devices. However, despite the well-established body of literature on semiconductor behavioral changes in the presence of grain boundaries, relatively little information exists addressing the existence of internal interfaces in FeS_2 and their effect on macroscopic material properties. Here we use high-resolution synchrotron x-ray diffraction to characterize the structure and composition of synthetic FeS_2 particles. Particles range in size and degree of polycrystallinity to investigate the surface and interfacial effects frequently associated with an imperfect material. We assess the magnetic and optical responses using SQUID magnetometry and ultraviolet-visible light absorption spectroscopy to better understand the macroscopic effects of grain boundaries on system properties. All particle sizes, ranging from nanometer to micrometer scale, are stoichiometric and phase-pure, with grain boundary density increasing with size. Additionally, there is a correlation between increasing particle size, magnetism onset, and decreasing optical band gap, which are explained by the increased interface presence identified in our structural analysis. Magneto-optical responses provide insight on the potential defect structures present at interfacial boundaries within FeS_2 solids.

Decades of research have been dedicated to the study of iron pyrite, FeS_2, in order to access its desirable semiconducting properties. What was initially an investigation into a promising photoabsorber has since evolved into a considerably complex materials problem. This is best illustrated by the material's electronic behavior: while reports of optical properties have indicated the presence of a band gap, E_g, near the expected value of 0.9 eV, electronic measurements show a much reduced E_g and integration into devices has been almost wholly unsuccessful.[1–4] Hampered electronic properties in iron pyrite are most generally associated with the deleterious effects of sulfur point-defects on band structure, which have been shown to induce localized electronic states within the forbidden gap.[5,6]

Comprehensive studies on FeS_2 with respect to defect structure chiefly consider single-crystal samples. Experimental studies rely on macroscopic manifestations of defect structure to understand both the nature of the defects and their effect on macroscopic properties. Reports on single crystal electrical properties have utilized Hall effect measurements to demonstrate the existence of a conductive inversion layer at the material surface, thus arguing for the overriding importance of surface sulfur vacancies in reduction of the band gap.[7] Others have used the electrochemical response of single crystal iron pyrite to assert that bulk vacancies play a more significant role in stunted electrical performance than vacancies existing at the surface.[8,9]

Despite considerable emphasis in the larger body of semiconducting literature to understand and control grain boundary effects, the specifics of these interfaces in iron pyrite have not been treated with this rigidity.[1,10–12] The presence of large scale internal defects such as grain boundaries and porosity result in syntheses of all kinds, encompassing both the nanoparticle and thin film approaches critical to efficient and scalable material generation. FeS_2 literature has noted the increased likelihood of grain boundaries as defect sinks and thus sites for potential vacancy aggregation even at compositions very near stoichiometry. Such experiments are corroborated by density functional theory work showing lower vacancy formation enthalpy at surfaces or interfaces.[7,12] However, material property changes owing to increased levels of polycrystallinity has not been sufficiently demonstrated.

[a] Department of Mechanical Engineering, University of Colorado at Boulder, Boulder, USA. E-mail: stoldt@colorado.edu
[b] National Institute of Standards and Technology, Boulder, USA.
[†] Electronic Supplementary Information (ESI) available. See DOI: 10.1039/b000000x/

As a response to this gap in the literature, we combine high resolution structural information from synchrotron x-ray diffraction (XRD) with sensitive magnetic and electronic measurements in order to assess possible contributions of internal surfaces in synthetic iron pyrite systems with increasing polycrystallinity. We look at particle size effects, with particle size varying by an order of magnitude, to make a distinction between grain boundary-specific phenomena and those associated with bulk or surface point-defects. Study of magnetic and optical behavior provides insight into potential structural features residing at internal surfaces and interfaces by assessing the electronic structure implied by measured responses. By systematically increasing both size and degree of polycrystallinity, we are able to provide a comprehensive picture of behavior induced by large scale internal defects, principally grain boundaries. While the ideal case would be to analyze particles created by a single synthesis type, generating a size range on the order of that presented herein through a single synthetic route is unfeasible. However, this constraint is taken into account as best possible when analyzing the source of measured responses. This allows us to comment on the interplay between length scale, defect structure, and the presence of interfaces.

1 Experimental methods

FeS_2 was synthesized using a close adaptation of a synthetic scheme previously published by Macpherson et al.[13] All chemicals were purchased from Sigma Aldrich and used without further refinement with the exception of $FeCl_2 * 4H_2O$, which was dehydrated under argon to achieve a $FeCl_2 * 2H_2O$ hydration state as verified by XRD. 600 mg of polyvinylpyrrolidone (PVP; average molecular weight = 10,000) was dissolved in 17 mL ethylene glycol. 127 mg $FeCl_2 * 2H_2O$, 8 mL 1 M NaOH, and 180 mg sulfur were stirred sequentially for 30 minutes in a glass vessel. The mixture was then heated dielectrically in a Discover SP (CEM, Inc.) microwave oven at 75 W until achieving 190 °C and was held at that temperature for 12 hours. The reaction was then cooled with compressed air. Methanol was added to the solution and the particles were separated by a washing process in which the solution was thrice centrifuged with methanol and the supernatant discarded. The resulting microparticle/methanol solution was dried under vacuum and the particles were transferred to an argon glovebox for air-free storage and future sample preparation. Small and mid-sized particles were synthesized using the protocols described by Macpherson et al. and Bi et al., respectively.[1,2]

High resolution synchrotron powder diffraction data were collected using beamline 11-BM at the Advanced Photon Source, Argonne National Laboratory, using an average wavelength of 0.0414621 nm. Measurements were taken from 2° to 50° 2θ, with data points collected every 0.001° 2θ and scan speed of 0.01°/s. The sample was placed in a capillary tube and loaded robotically into the beamline. Such geometry avoids preferred orientation problems, which can affect the quality of subsequent refinements. Rietveld refinement of the data was performed through the EXPGUI interface of the General Structure Analysis System software.[10] Williamson-Hall analyses are used to analyze particle size while accounting for strain potential within the particles. Scherrer constants used in these analyses are chosen with respect to particle shape as defined by Langford et al.[14] Spherical nanoparticles use the spherical full-width half max (FWHM) approximation of $K_w = 0.94$; for mid-sized, square nanoparticles, K_w is averaged over the listed reflections for cubic crystallites to obtain a value of 0.88; and for micron-scale particles, an averaged K_w for octahedral crystallites of 0.88 is used.

Scanning electron microscopy images were generated using a Hitachi SU3500 microscope with a 5.00 kV generating voltage and a working distance of 5.7 mm. Energy dispersive x-ray spectroscopy (EDS) was performed on a JEOL JSM-6480LV scanning electron microscope (SEM). Particles dispersed in chloroform were drop-cast on a silicon plate and the solvent was evaporated. The sample was then immediately placed in the SEM under vacuum. Composition was taken in several places for both nanoparticles and microparticles and averaged. No oxygen was detected.

Magnetometry and AC susceptibility data were taken at the National Institute of Standards and Technology in Boulder, Colorado (NIST-Boulder) on a Quantum Design MPMS 7. Each set of measurements was taken in a single session. Full magnetic measurements were taken on different batches of particles produced from repeated syntheses and showed consistent magnetic behavior at each particle size. Sample preparation was as follows: 23 mg FeS_2 powder stored under argon was weighed and transferred to a 10 cm long section of single-sided Kapton tape. The Kapton was then folded on itself to seal the particles inside. The sample was transported under argon to NIST, where it was removed and inserted into a plastic straw for installation in the magnetometer. This was the only time where the nanoparticles may have had air exposure; Kapton has a relatively low permeability to air. Once in the magnetometer, three pump/purge cycles replaced residual air with high purity helium. The length for the segment of Kapton was chosen such that the boundaries of the tape never exited the measurement segment of the magnetometer; therefore, any signal from the Kapton was canceled due to symmetry. For details on the field and frequency used for these measurements, please refer to images and text below.

Absorption measurements via ultraviolet-visible (UV-vis) spectroscopy were obtained using a Shimadzu 3101 spectrophotometer. Microparticles were ligated with oleylamine and suspended in chloroform. The background signal of chloroform and glass cuvette were used as reference spectra. Nanoparticles were dispersed in chloroform without ligation. In order to determine if significant effects on measured absorption occurred as a result of attached oleylamine ligands, we compared our results to FeS_2 particles with oleic acid ligands attached (see Supplementary Information). No significant differences were detected.

2　Results and discussion

To better elucidate the nature and consequences of defect structure on FeS_2, it is necessary to consider the material across length scales. To this end, this study presents three different particle syntheses designed to produce FeS_2 at sizes ranging from the nanometer to micrometer scale. What follows is a comprehensive comparative analysis that evaluates the impact of a systematically varying defect structure with particle size on macroscopic magnetic and electronic properties. For nanometer scale materials, it is assumed that most defects present in the system are exuded to the material surface during growth. As particle diameter increases, however, so too does the diversity of defect types available within the system. As the volume-to-surface ratio increases, so too does the propensity to trap point and linear defects within the bulk. Similarly, interfacial defects such as grain boundaries become more prevalent with increasing particle size. By tailoring our syntheses to generate particles of increasing diameter, systematic structure-property relationships can be elucidated with the goal of connecting the underlying defect structure, evidenced by crystallography and microscopy, to measured magnetic and optical behavior.
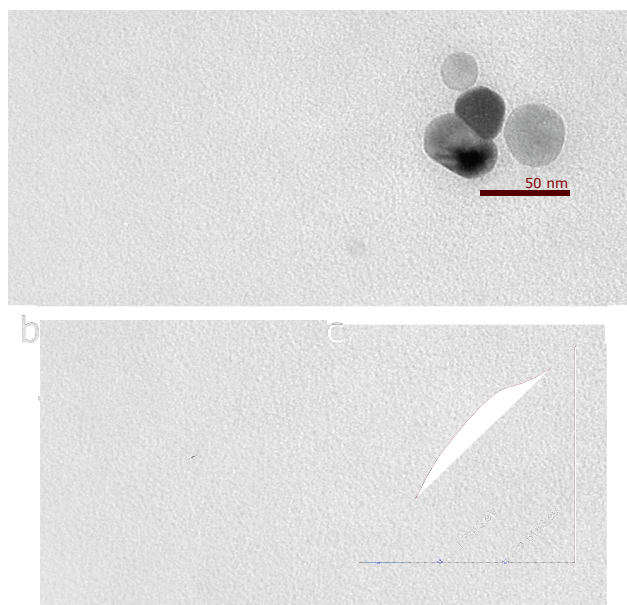

Fig. 1 (a) Synchrotron XRD with refinement (red dashed line) and TEM (inset), (b) magnetic, and (c) Tauc plot of optical data from the FeS_2 nanocrystals having a measured diameter of approximately 25 nm. The x-intercepts in the Tauc plot represent indirect and direct band transitions.

2.1　Small-sized Particles

FeS_2 nanocrystals were synthesized to be representative of a surface-area-dominant single crystalline species lacking the interfacial boundaries generally prevalent in larger-scale solids. The results of our structure-property analysis for this length scale are shown in Figure 1. In order to assess the crystallinity and phase purity of our resulting product, we utilize synchrotron XRD obtained using the BM-11 beamline at Argonne National Labora-

tory. The lower wavelengths associated with synchrotron XRD allows for higher resolution measurements with an experimental setup, minimizing adverse effects from preferred orientation and iron fluorescence that can plague laboratory scale diffractometers. [11,15,16] The synchrotron XRD pattern in Figure 1a shows diffraction peak locations for the nanocrystals that are in excellent agreement with those expected for cubic iron pyrite A reference pattern for comparison is provided in the Supplemental Information (SI). These nanocrystals are determined to be phase pure to the detection limits of the measurement, with no visible presence of the impurity phases commonly cited in literature, namely crystalline non-stoichiometric monosulfides ($Fe_{(1-x)}S$) or marcasite (orthorhombic FeS_2).

The inset in Figure 1a shows a representative transmission electron microscopy (TEM) image of the solvothermally-prepared material, which presents a near-spherical morphology with no evident intra-particle features commonly associated with higher order structure such as line defects or grain boundaries. Size distributions for all three particle systems were determined by analysis of microscopy images; the results of these analyses are shown in the Supporting Information. As is often reported in nanoparticle systems, a lognormal distribution is observed for both small and medium-particles. [17,18] A Williamson-Hall analysis, shown in Figure 4, was performed using synchrotron XRD data to determine an approximate crystallite size in the product. The effects of machine broadening are minimized by the highly monochromatic nature of the synchrotron beam and by the use of provided instrumental files accounting for machine-related effects. This analysis was performed using the same synchrotron data over 20 reflections to understand size and strain within the particles. The analysis yielded a crystallite size of approximately 23 nm and small strain on the order of 10^{-3}, which is consistent with the particle dimensions observed by TEM and thus suggestive of a nominally single crystal product.

The results of a Rietveld refinement of the synchrotron XRD data shown in Figure 1a provide an estimate of the material composition of the FeS_2 nanocrystals described above. The refinement determined the nanocrystals to be essentially stoichiometric, with a composition of $FeS_{1.99}$. Rietveld refinement techniques utilize a least squares routine to determine crystallographic parameters the produce a diffraction pattern that best approximates experimental data. Fit quality is determined by calculated goodness of fit parameters, including a χ^2 value near but not below unity, and by a visual comparison of fit to data. [16] Our nanocrystal refinement gives a $\chi^2 = 4.50$, $wR_p = 0.104$, and a fit in good agreement with experimental peak and background locations; thus, we believe the occupancy values derived from our refinement to be trustworthy. A summary of structural data and goodness of fit parameters from each refinement is shown in Table 1, where x(S) and x(Fe) are the lattice location of sulfur and iron atoms respectively and S_{occ} is the occupancy of sulfur in its lattice position. The x, y, and z coordinates of sulfur and atom were equal for respective atoms in all refinements. To further verify composition values, we performed energy dispersive x-ray spectroscopy (EDS) on all samples. Composition was taken at various points on a drop cast film of nanocrystals. Through an averaging

of these data points, we estimate a composition of $FeS_{2.09+/-0.12}$, supporting the notion of a stoichiometric particle given by the refinement result.

Next, we report high-sensitivity SQUID magnetometry on our single crystal nanoparticles to measure low- and room-temperature magnetism. Figure 1b shows the mass magnetization (M) as a function of applied magnetic field ($\mu_0 H$) for the FeS_2 nanocrystals at 1.8 K, 35 K, and 300 K. At room temperature, different batches of particles synthesized under the same procedure show primarily diamagnetism or, to a lesser degree, very weak paramagnetic behavior. Our room temperature results are consistent with expected behavior and supported by orbital models proposed by Tributsch et al. using crystal field theory.[19–21] In non-defective pyrite, the octahedrally coordinated iron is expected to be in a low spin 2^+ state, and it has been determined that the magnetic state of iron pyrite is driven by d-orbital iron electrons - thus, an ideal system should display diamagnetic behavior with all 6 valence electrons paired in the three t_{2g} orbitals.[8] In our nanocrystal specimen, paramagnetic and antiferromagnetic components are reproducibly shown at 1.8 K. The paramagnetic component is seen by the Langevin-like response at 1.8 K, while the antiferromagnetic behavior is seen by continual increase in moment at high fields, where the paramagnetic response is saturated. A superparamagnetic phase transition, as demonstrated by slope changes in zero-field cooled (ZFC) and field-cooled (FC) measurements, appears between 20 and 40 K (see SI), and signals a transition from thermally fluctuating magnetic clusters to fixed moment clusters at low temperatures. The low temperature magnetic response (Fig. 1b) is interpreted as a paramagnetic component due to the reorientation of the magnetic cluster moments, along with an antiferromagnetic component due to moment alignment within the strongly exchange coupled clusters. There is precedent for this type of behavior in the synthetic pyrite literature for particles with diameters less than 100 nm, behavior attributed to localized non-stoichiometric phases in the solid, namely pyrrhotites, that become macroscopically evident at lower temperatures due to a decrease in thermal fluctuations.[22,23] These reports, however, do not explore composition nor quantitatively treat structure in their assessment. We believe that measured variation across batches of material may be attributed to inevitable environmental exposure which forms surface species such as $FeS_2(SO_4)_3$, FeOOH and Fe_2O_3 - oxidation products of pyrite that display antiferromagnetism and ferromagnetism.[24,25] While the nanocrystals described here are protected from air exposure as best as possible, transfer to the magnetometer still presents an opportunity for environmental exposure given the very high surface area of the nanocrystals.

Nanocrystal UV-visible absorbance was also evaluated to further our understanding of the electronic environment within FeS_2 particles. Tauc plots are generated from absorbance data across the UV-visible range to determine energetic locations of electronic direct and indirect band transitions, the results of which are plotted in Figure 1c. As-acquired absorption data is given in the SI. Single crystal nanoparticles show the single indirect and multiple direct band transitions at about 1.00, 1.78, and 2.62 eV, respectively. While significant variation has been reported across syn-thetic pyrite samples, our indirect and direct gaps align well with computational treatments of non-defective pyrite, furthering our position that the nanocrystals represent a near ideal pyrite product.[2,26,27]

When considered alongside magnetic data, the optical results reported here suggest a high-quality, stoichiometric product that closely approximates the properties of theoretical pyrite. Due to their near-ideal behavior, the nanocrystals are used as the basis of comparison to the following specimen where the average particle diameter is systematically increased through changes to the synthetic protocol.

Table 1 Rietveld refinement results for each particle size. Crystallite size is derived from synchrotron data through the Williamson-Hall analysis described above.

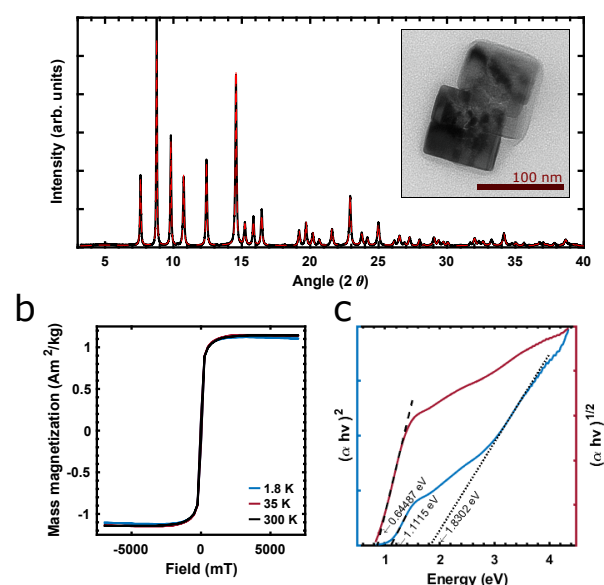| Avg size (nm)	Avg cryst size (nm)	a (nm)	x(S)	x(Fe)	S_{occ}	χ^2	wR_p
27.5±9	22.9±2	0.54216	0.3850	0.000	0.99	4.498	0.1038
72.7±23	33.2±10	0.54216	0.3841	0.000	0.98	3.357	0.1010
883.5±199	385.0±165	0.54206	0.3849	0.000	1.00	1.085	0.1487

Fig. 2 (a) Synchrotron XRD with refinement (red dashed line) and TEM (inset), (b) magnetic, and (c) Tauc plot of optical data from the FeS_2 nanocrystals having a measured side length of approximately 75 nm.

2.2 Medium-sized particles

We next assessed a slightly larger nanoparticle in order to probe the behavior of FeS_2 in a size range that bridges the gap between bulk- and surface-dominated behavior, i.e., between the nanoscale and microscale. The inset in Figure 2a shows our solvothermally-synthesized particles have a fused-cube morphology and average edge length on the order of 100 nm. Repeated measurements and careful sample preparation lead us to believe that the fused nature of these particles is indicative of their true morphology, as supported by the Williamson-Hall analysis, rather than being an artifact of TEM sample preparation. The repre-

sentative synchrotron XRD pattern, shown in Figure 2a, shows our particles to again be phase pure within detection limits when compared to reference data for FeS_2. The Williamson-Hall analysis of synchrotron XRD data from Figure 2a, plotted across 20 reflections, finds the particles to be composed of 33 nm crystallites, which, compared to the overall particle size measured by TEM, signals a degree of polycrystallinity not found in the small-sized particles. A very small strain on the order of 10^{-3} is also calculated by this method. As with the smaller nanocrystals, the solvothermal process used here generates primary particles having a diameter of about 23 nm, however, through a different ligand chemistry, these primary particles are able to coalesce during equilibration yielding a medium-sized aggregate composed of fused primary particles.

Like the nanocrystals, a Rietveld refinement fitted to experimental synchrotron XRD data yields a similar stoichiometry, giving a chemical formula of $FeS_{1.95}$ with goodness of fit parameters $\chi^2 = 3.36$ and $wR_p = 0.101$, again providing confidence in calculated refinement values. Compositional analysis determined by EDS gives a similar result of $FeS_{2.17 +/- 0.11}$, which again indicates no significant non-stoichiometry in our specimen, notably no sulfur deficiency.

SQUID magnetometry taken on the mid-sized FeS_2 particles is given in Figure 2c and shows ferromagnetic behavior at all temperatures, consistent with the absence of a magnetic phase transition seen in the corresponding zero field cooled (ZFC) and field-cooled (FC) measurements (provided in the SI). Magnetic saturation consistently occurs around 2.0 T for the batches of mid-sized particles evaluated by SQUID. A response of this kind is not unusual in synthetic pyrite literature; however, it definitely marks a divergence from the hallmarks of ideal pyrite behavior discussed previously. Ferro- or antiferromagnetism dictates the presence of unpaired spins in the sample; thus, all electrons within our particle system cannot be in the low-spin Fe^{2+} electronic configuration. Other reports on synthetic iron pyrite reason the source of magnetism to be the result of either dangling bonds or miniscule quantities of impurity phases such as $Fe_{(1-x)}S$, the latter previously shown to be ferromagnetic or antiferromagnetic. While it is possible for very small quantities of crystalline impurities to be present below the detection limit of the synchrotron X-ray diffractometer, the systematic absence of detectable impurity phases across all three specimen sizes and trials compel us to explore other sources of magnetism in these particles. Namely, we must assume that unpaired spins reside either at point defects or at buried interfaces within the system's bulk volume.

Tauc plots generated from an absorption measurement on the mid-sized particles, shown in Figure 2c, are consistent with perturbed electronic effects evidenced by our magnetometry results. The indirect and first transitions are reduced to 0.64 eV and 1.11 eV, respectively. A reduced bandgap in synthetic FeS_2 is generally reported to be a result of systemic sulfur vacancies which induce defect states within the forbidden gap; however, this interpretation alone may provide an incomplete picture of particle behavior as it does not consider interfacial effects.[7–9] In order to explore these possibilities further, we move to an assessment of micron-scale particles.
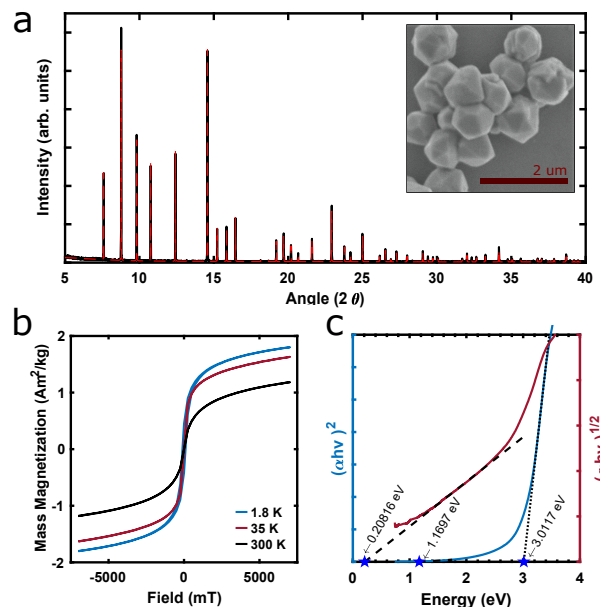

Fig. 3 Structural (a), SEM (inset), magnetic (b), and optical (c) data represented as a Tauc plot for large microparticles with sizes on the order of 1 μm and a morphology that blends cubic and octahedral elements. The red curve a) shows the Rietveld refinement fit for the synchrotron XRD data shown in black.

2.3 Large-sized particles

The inset of Figure 3a shows a typical SEM image of microparticles generated by a hydrothermal process, one that is significantly different than those described previously. Here, we adopt a hydrothermal synthesis that utilizes microwave heating, since there is an inherent limitation to achieving larger-sized particulates in ligand-dense solvothermal environments such as those used to generate the small- and medium-sized particles. The microparticles, with an average diameter of 883 nm, are highly faceted and clearly polycrystalline, appearing to be an agglomeration of many smaller units that combine both tetrahedral and octahedral elements. A size distribution for these particles is included in the SI. The associated synchrotron XRD pattern given in Figure 3a indicates a pure-phase product within detection limits of the instrument, showing no traceable presence of any secondary crystalline phases. From this data, a Williamson-Hall analysis assessing 20 reflections gives an estimated crystallite size on the order of 385 nm with minimal strain on the order of 10^{-4}. It is notable that the extracted particle size is less than half that of the particle size observed by SEM, indicating that these particles are also likely composed of multiple crystalline grains. As with all diffraction analyses in this work, the effects of line broadening are minimized due to the use of synchrotron wavelengths with well characterized instrument parameters. A polycrystalline product with this morphology is not inconsistent with literature models of pyrite growth, in which agglomeration and coalescence of smaller particles precedes recrystallization into a larger, single crystalline material.[28]

Surprisingly, the refinement of the XRD data reports the microparticles to be stoichiometric and of a similar makeup to the smaller-sized specimen discussed previously; a composition of

$FeS_{2.00}$ is determined with a $\chi^2 = 1.085$ and $wR_p = 0.1487$. EDS measurements are reflective of this near-ideal stoichiometry, giving a composition of $FeS_{2.038+/-0.10}$ averaged across several measurement locations.
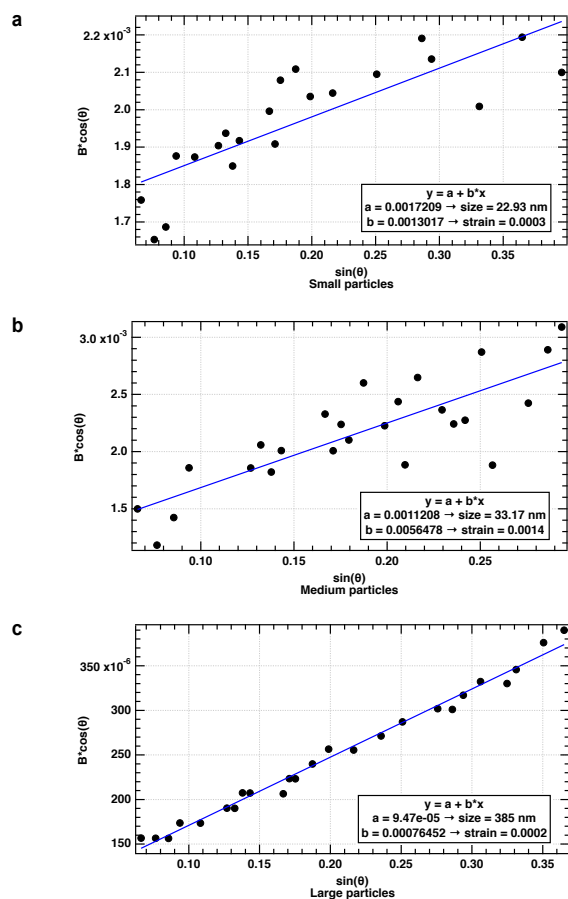

Fig. 4 Williamson-Hall analysis of a) small, b) medium, and c) large particles using information from synchrotron XRD patterns.

SQUID magnetometry measurements reported in Figure 3b for the microparticles show a higher magnitude magnetism than measured for any of the smaller sized samples. Further, the data shows superparamagnetic and potentially antiferromagnetic behavior at all three temperatures evaluated, as indicated by the absence of hysteresis in the curves. While some researchers have reported seeing superparamagnetism in size-limited diamagnetic materials, for example in Ag and Au nanoparticles, these assertions remain controversial.[29–31] The few existing reports of superparamagnetism in diamagnetic bulk materials relate to particles on the order of 10 nm, many orders of magnitude smaller than the microparticles reported here.[32] Thus the superparamagnetic response measured in the microparticles does not likely result from effects related to a stoichiometric, diamagnetic solid, but is instead derived from unpaired electrons in the as-synthesized material.

The increase in magnetic moment, approximately 20 times that of the smaller nanoparticles reported in Figure 1b, correlated with the the difference in magnetic response between the midsized nanoscale and 1 μm particles, can be understood through the temperature-dependent magnetization information gleaned from ZFC and FC measurements (provided in the SI). Spontaneous magnetization is present in our system as evidenced by the non-zero moment as temperature approaches 0 K, indicating that the system is slightly ferrimagnetic. The presence of slight ferrimagnetism in antiferromagnetic particles has been attributed to the scale of the permanent magnetic moment formed by differing number of components in magnetic sublattices forming the crystal. The magnitude of this moment is inversely proportional to the size of the particle; thus, in smaller particles ferromagnetism is more likely to be macroscopically evident than in larger particles, where mutual cancellation of individual moments occurs on a larger scale.[29] We believe the magnetic responses in our 100 nm and 1 μm particles to be well described by this phenomenon.

Tauc plots generated from an absorption measurement on the microparticles, shown in Figure 3c, corroborate this significant deviation from pyrite's ideal electronic state, with a measured indirect bandgap of about 0.21 eV, significantly reduced from the "ideal" indirect gap of approximately 1.0 eV reported in Figure 1c. The presence of band tailing is also more apparent here than in the two nanoscale systems. This signals an increase in electronic disorder, which can among other things be induced by intrinsic defects such as vacancies and dislocations or from extrinsic defects such as doping and off-stoichiometry.[33]

Table 2 Magnetic responses from synthetic iron pyrite as reported in literature. * indicates results from this work.

Size (nm)	Morphology	Growth Method	Magnetism at RT	Ref
10-26	Spheres	Autoclave	AF	[22]
13-34	Ellipsoids	Autoclave	FM	[22]
20	Spheres	Solvothermal	DM/PM	*
70	Plates	Hydrothermal	FM	[34]
70-150	Cubes	Hydrothermal	DM	[21]
100	Cubes	Hydrothermal	FM	*
100	Spheres	Sulfidized film	FM	[35]
300	Octahedrons	Solvothermal	AF	[36]
300	Cubes	Solvothermal	PM	[36]
500	Spheres	Autoclave	FM	[22]
1000	Octahedrons	Hydrothermal	AF	*

2.4 Magnetism and interfacial boundaries

For all particle sizes, our composition data shows near-ideal stoichiometry that belies the presence of a significant population of point defects within the bulk. Instead, the variation in stoichiometry across all particle sizes remains negligible, suggesting that FeS_2 as prepared here maintains at most a very small intrinsic point defect population. This observation is critical in this study, as it indicates that we cannot reasonably ascribe bulk point defects as the principal source for deviant magneto-optical properties, as is often argued in FeS_2 literature.

Our results instead point to the need for a more thorough assessment of other structural motifs that result from kinetically controlled synthetic processes; namely, the effect of interfacial defects on the overall material behavior of iron pyrite. In our systematic study of particle size, we also see an increase in interfacial area given by increasing number of crystallite grains in a given particle size as determined by respective Scherrer analyses. Inter-

facial defects including line, stacking faults, and grain boundaries have long been noted for their adverse effects on measured material properties, particularly in the semiconductor industry, so it is not unreasonable that these effects can play a role in the macroscopic behavior measured here as well. Furthermore, it is often the case that such types of defect structure are under-emphasized due to the inherent challenge in their detection, characterization, modeling, and interpretation.

Across the size range encompassed by our particles, the bulk composition is found to be nominally stoichiometric as determined by both Rietveld refinement, quantitative x-ray analysis, and EDS. Therefore, we must look beyond non-stoichiometry for the source of the increased magnetic moment and reduced optical gap at larger particle diameters. With increasing size, we definitively find an increase in the number of grains per particle, and therefore the number of grain boundaries present. An estimate of the total grains per particle gives that our smallest sized particles are single crystalline in nature, having on average one grain per particle. This conclusion is confirmed by TEM analysis. Mid-sized particles have on the order of 10^1-10^2 grains per particle given an average grain size of about 33 nm. Lastly, the largest-sized, 1-2 μm diameter particles contain on the order of 10^1-10^2 grains per particle given their larger average grain size of about 385 nm. A corresponding increase in interfacial surface area comes with the increasingly polycrystalline nature of our products and can plausibly serve as a contributing source to the macroscopic deviations from ideal behavior reported here. Using a simplified model of particle makeup from the grain sizes determined by our Williamson-Hall analyses (see SI), we estimate significant increases in interfacial surface area with increasing particle size. While the smaller nanoparticles are single crystalline and have no interfacial surface area, the interfacial surface area found in a microparticle is a significant portion, upwards of 90%, of the area attributed to its external surfaces only. Thus far, this analysis has only considered the impact of internal interfaces residing at grain boundaries. In the microwave synthetic environment, the microscale particle results from agglomeration processes during growth and equilibration. Therefore, the presence of other larger scale internal defects such as pores, voids, and inclusions is possible. In point of fact, porosity in hydrothermal FeS$_2$ syntheses of this size are previously shown to exhibit a degree of surface porosity. [37,38], which is subsequently integrated into the larger agglomerate as internal porosity. While not explicitly analyzed herein, some degree of porosity is anticipated in the larger particles in addition to grain boundaries, and we should therefore not discount such defect structure as a contributor to the observed behavior at the microscale.

Given the nature of measured variation in magneto-optical properties with increasing polycrystallinity in our samples, it is reasonable to focus our attention on intraparticle interfacial defects as a potential root cause. We argue that the effects of defects at external surfaces such as vacancies are unlikely to play a major role in this discussion. If a dilute number of external surface sulfur vacancies were sufficient to produce an electronic signature, we would expect to see this more strongly reflected in our smallest nanoscale specimen where surface area vastly outpaces

bulk volume; however, it is this specimen that exhibits behaviors most ideal. This topic is discussed in more detail in the following section.

2.5 Candidate structure and chemistry at grain boundaries in synthetic FeS$_2$

Amorphous content at grain boundaries has been reported in nanoparticle systems; as an example, superparamagnetic Fe-(O)H content could plausibly lie in the boundary of hydrothermally-derived microparticles. [39,40] These cases can also provide the conditions necessary to disturb optical properties. [41–43] While we acknowledge that the presence of amorphous material is not directly explored in this work due to the inherent challenges in its detection, the presence of amorphous content is supported in that our XRD data presents a high quality, stoichiometric crystalline product that may preclude a population of unpaired electrons from sulfur vacancy point defects sufficient for a bulk magnetic response.

In addition to serving as point defect sinks, interfacial regions such as grain boundaries, porosity, voids, and inclusions are ripe for lattice mismatch, strain defects, and line defects. [32] Off-stoichiometric crystalline content gathered in these regions could be non-diamagnetic, as pyrrhotites are often found to be ferromagnetic or anti-ferromagnetic. The presence (or inferred presence) of impurity phases is commonly cited in the literature as a source of magnetic response measured in synthetic FeS$_2$. [7,9,12] Magnetic signatures in zero-field cooled curves of FeS$_2$ nanoparticles have been attributed to the presence of pyrrhotite, but these assignments are debatable as at least one of the peaks discussed in literature has since been determined to be an instrumental artifact. [44] Products of mixed phase have been shown to reduce the band gap of a material in spectroscopic measurements. The FeS$_2$ literature has addressed the possibility of a conductive pyrrhotite-like "shell" existing about a nanoparticle that essentially limits its performance. [43] The presence of impurity atoms may also have an effect on absorbance behavior; for example, a red-shift in absorbance data has been shown in nitrogen-doped TiO$_2$. [41,42] We believe this latter case to be unlikely in our particle systems as the result is not magnified in our surface-dominant nanocrystal specimen. Other works have proposed the presence of unreacted crystalline precursor in FeS$_2$ materials as the source of magnetic response in synthetic FeS$_2$, but these claims are structurally and compositionally unconfirmed. A compilation of magnetic results reported in iron pyrite literature is presented for completeness in Table 2, demonstrating significant magnetic property variation with synthetic approach and product morphology and scale.

In FeS$_2$ syntheses such as those described, grain boundaries and other large scale defects form as the result of irreversible collisions between individual particles in the growth medium. [36] These internal interfaces, unlike external interfaces, are kinetically trapped and limited in their ability to further equilibrate. Thus, internal interfaces are likely to exhibit higher grain boundary angle, higher strain, and non-stoichiometry. While the S-terminated 100 surfaces are calculated to be of lowest free energy with a band gap near ideal, other higher free energy interface ter-

minations in FeS$_2$ are found to be electronically conductive, a likely possibility for non-equilibrated surface structure formed at grain boundaries.[45,46] Due to the inherent limitations of XRD in the analysis to 2-D layers, localized non-stoichiometry including under-coordinated iron and amorphous content or phase impurities of this ultra-thin nature would be undetectable by the methods used here. However, this complex and variable interfacial environment provides a likely source for the magnetic discrepancy between our particles of high polycrystallinity and the diamagnetic response expected in stoichiometric iron pyrite. Similarly, this environment can facilitate the diminished opto-electronic properties exhibited across length scales in our FeS$_2$ materials.

3 Conclusions

We present a study of large scale defect structure, principally grain boundaries, in synthetic iron pyrite through a rational, size-based approach, coupled with optical and magnetic measurements to characterize property variation with increasing scale. Structural information determined by synchrotron XRD is viewed alongside a sensitive assessment of each system's magnetic response and electronic transitions via SQUID magnetometry and UV-visible spectroscopy respectively. Our experimental approach allows isolation of the contributions of grain boundary and other large scale defect structure on system-wide macroscopic properties in the pyrite system. Surprisingly, the smallest particles, with dimensions around 25 nm, showed the most ideal response, while larger particles showed magnetic and optical responses indicative of intra-particle interfacial defects. Rational increase of size allows an evaluation of defect structure that helps clarify the diverse reports of the effects of sulfur defects in iron pyrite literature. By better understanding the consequences of large scale defect structure, syntheses of pyrite can be manipulated to eliminate or take advantage of interfacial pathways in the pursuit of successful energy applications.

3.1 Conflict of Interest

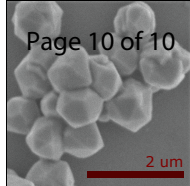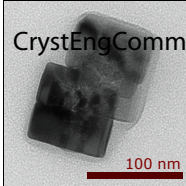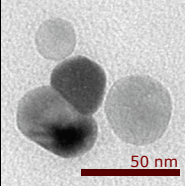There are no conflicts of interest to declare.

3.2 Acknowledgements

References

1 Y. Bi, Y. Yuan, C. L. Exstrom, S. A. Darveau and J. Huang, *Nano Letters*, 2011, **11**, 4953–4957.

2 H. A. Macpherson and C. R. Stoldt, *ACS Nano*, 2012, **6**, 8940–8949.

3 A. Kirkeminde, R. Scott and S. Ren, *Nanoscale*, 2012, **4**, 7649.

4 A. Ennaoui and H. Tributsch, *Solar Energy Materials*, 1986, **14**, 461–474.

5 M. Bronold, C. Pettenkofer and W. Jaegermann, *Journal of Applied Physics*, 1994, **76**, 5800–5808.

6 A. Ennaoui, S. Fiechter, W. Jaegermann and H. Tributsch, *Journal of The Electrochemical Society*, 1986, **133**, 97–106.

7 M. Limpinsel, N. Farhi, N. Berry, J. Lindemuth, C. L. Perkins, Q. Lin and M. Law, *Energy & Environmental Science*, 2014, **7**, 1974.

8 M. Birkholz, A. Hartmann, S. Fiechter and H. Tributsch, *Tenth E.C. Photovoltaic Solar Energy Conference*, Springer, Dordrecht, 1991, pp. 96–99.

9 M. Cabán-Acevedo, N. S. Kaiser, C. R. English, D. Liang, B. J. Thompson, H.-E. Chen, K. J. Czech, J. C. Wright, R. J. Hamers and S. Jin, *Journal of the American Chemical Society*, 2014, **136**, 17163–17179.

10 A. Larson and R. Von Dreele, *Los Alamos National Laboratory Report LAUR 86-748*, 2000.

11 J. Ward, *Rev. Pure Appl. Chem.*, 1970, **20**, 175–206.

12 L. Yu, S. Lany, R. Kykyneshi, V. Jieratum, R. Ravichandran, B. Pelatt, E. Altschul, H. Platt, J. Wager, D. Keszler and A. Zunger, *Adv. Energy Mater.*, 2011, 6.

13 T. A. Yersak, H. A. Macpherson, S. C. Kim, V.-D. Le, S. K. Chan, S.-B. Son, Y.-H. Kim, J. E. Trevey, K. H. Oh, C. R. Stoldt and S.-H. Lee, *Adv. Energy Materials*, 2013, **3**, 120–127.

14 J. I. Langford and A. J. C. Wilson, *Journal of Applied Crystallography*, 1978, **11**, 102–113.

15 D. Rickard and G. W. Luther, *Chemical Reviews*, 2007, **107**, 514–562.

16 B. Toby, *J. Appl. Crystallogr.*, 2001, **34**, 210–213.

17 M. Blanco-Manteco and K. O'Grady, *Journal of Magnetism and Magnetic Materials*, 1999, **203**, 4.

18 J. C. Thomas, *Journal of Colloid and Interface Science*, 1987, **117**, 187–192.

19 S. Miyahara and T. Teranishi, *Journal of Applied Physics*, 1968, **39**, 896–897.

20 P. A. Montano and M. S. Seehrat, *Solid State Comm.*, 1976, **20**, 897–898.

21 V. P. Gupta and N. M. Ravindra, *Solid State Comm.*, 1979, **32**, 1327–1328.

22 S. Shukla, G. Xing, H. Ge, R. R. Prabhakar, S. Mathew, Z. Su, V. Nalla, T. Venkatesan, N. Mathews, T. Sritharan, T. C. Sum and Q. Xiong, *ACS Nano*, 2016, **10**, 4431–4440.

23 J. Xia, J. Jiao, B. Dai, W. Qiu, S. He, W. Qiu, P. Shen and L. Chen, *RSC Advances*, 2013, 9.

24 S. Karthe, R. Szargan and E. Suoinen, *Appl. Surf. Sci.*, 1993, **72**, 158–170.

25 A. Yamamoto, T. Honmyo, N. Hosoito, M. Kiyama and T. Shinjo, *Nuc. Instrum. Methods Phys. Res.*, 1993, **B76**, 202–203.

26 Q. Guanzhou, X. Qi and H. Yuehua, *Computational Materials Science*, 2004, **29**, 89–94.

27 L. Vadkhiya and B. L. Ahuja, *Journal of Alloys and Compounds*, 2011, **509**, 3042–3047.

28 M. Gong, A. Kirkeminde and S. Ren, *Sci. Rep.*, 2013, **3**, year.

29 H. Hori, Y. Yamamoto, T. Iwamoto, T. Miura, T. Teranishi and M. Miyake, *PHYSICAL REVIEW B*, 2004, **69**, 174411.

30 K. S. Krishna, P. Tarakeshwar, V. Mujica and C. S. Kumar,

Small, 2014, **10**, 907–911.

31 G. L. Nealon, B. Donnio, R. Greget, J.-P. Kappler, E. Terazzi and J.-L. Gallani, *Nanoscale*, 2012, **4**, 5244–5258.

32 M. Knobel, W. C. Nunes, L. M. Socolovsky, E. D. Biasi, J. M. Vargas and J. C. Denardin, *J. Nanosci. Nanotechnol.*, 2008, 22.

33 I. Studenyak, M. Kranjcec and M. Kurik, *Int. J. Opt. Appl.*, 2014, **4**, 76–83.

34 B. Li, L. Huang, M. Zhong, Z. Wei and J. Li, *RSC Advances*, 2015, **5**, 91103–91107.

35 Y. N. Zhang, M. Law and R. Q. Wu, *The Journal of Physical Chemistry C*, 2015, **119**, 24859–24864.

36 D.-W. Wang, Q.-H. Wang and T.-M. Wang, *CrystEngComm*, 2010, **12**, 755–761.

37 L. Liu, Z. Yuan, C. Qiu and J. Liu, *Solid State Ionics*, 2013, **241**, 25–29.

38 D. Zhang, J. P. Tu, J. Y. Xiang, Y. Q. Qiao, X. H. Xia, X. L. Wang and C. D. Gu, *Electrochimica Acta*, 2011, **56**, 9980–9985.

39 P. Gütlich and H. A. Goodwin, *Top Curr. Chem.*, 2004, 1–47.

40 M. Iacob, *RSC Advances*, 2015, 8.

41 C. Burda, Y. Lou, X. Chen, A. C. S. Samia, J. Stout and J. L. Gole, 2003, **3**, 1049.

42 A. Zachariah, K. V. Baiju, S. Shukla, K. S. Deepa, J. James and K. G. K. Warrier, *J. Phys. Chem. C*, 2008, **112**, 11345–11356.

43 L. Chen, W. Zhao, Y. Jiao, X. He, J. Wang and Y. Zhang, *Spectrochimica Acta A*, 2007, **68**, 484–490.

44 D. Harries and F. Langenhorst, *Meteoritics and Planetary Sciences*, 2013, **48**, 25.

45 A. Barnard and R. S.P., *J. Mater. Chem.*, 2013, **19**, 3389–3394.

46 D. Alfonso, *J. Phys. Chem. C*, 2010, **114**, 8971–8980.